Toward Air Stability of Efficient Filter-Free Band-Selective Organic Photodetectors Based on Bulk Heterojunction: Avoiding Environmental Degradation with Atomic Layer Deposition Encapsulation

Quentin Eynaud, Mohamed El Amine Kramdi, Vyshnav Kannampalli, Tomoyuki Koganezawa, Noriyuki Yoshimoto, Lionel Santinacci, Jörg Ackermann, Christine Videlot-Ackermann

ADVANCED ENERGY & SUSTAINABILITY RESEARCH
www.advenergysustres.com

Toward Air Stability of Efficient Filter-Free Band-Selective Organic Photodetectors Based on Bulk Heterojunction: Avoiding Environmental Degradation with Atomic Layer Deposition Encapsulation

*Quentin Eynaud, Mohamed el Amine Kramdi, Vyshnav Kannampalli, Tomoyuki Koganezawa, Noriyuki Yoshimoto, Lionel Santinacci, Jörg Ackermann, and Christine Videlot-Ackermann**

To detect the band-specific optical signals used in many fields, it is necessary to develop spectrally selective photodetection. For such wavelength-selective photodetection or color discrimination, organic photodetectors (OPDs) can offer significant benefits as low temperature and solution processability, chemical versatility, and specific spectral detection range. However, to avoid commonly used filters, the design of a narrowing approach that simultaneously achieves a selective detection range with a bandwidth of less than 50 nm and a spectral response of over 20% remains a challenge. OPDs based on charge-collection-narrowing principle can provide these features. In this approach, the detection window can be selected to match the absorption onset of the junction materials used in the bulk heterojunction layer. Herein, filter-free band-selective OPDs are realized based on PM6:$PC_{70}BM$ blends as state of the art. Fine adjustment over a bandwidth of 42 nm to be highly selective at 677 nm with a quantum efficiency of 48.4% under an inverse low bias of −2 V is reached. In addition, using a non-invasive and nondestructive encapsulation technique, it is demonstrated that these OPDs fully retain their high selective peak after 30 days storage in air.

1. Introduction

Photodetector (PD) has evolved into one of the key components of modern life, with numerous applications as image sensing, optical communication, and health/environmental monitoring. Specifically, spectrally selective photodetection has been largely employed in biomedical monitoring, artificial intelligence imaging, and surveillance, where only band-specific optical signals are intended to be detected.[1] While broadband PDs based on inorganic materials can reach a very wide range of the electromagnetic spectrum and achieve high detection, organic based PDs are not to be outdone, with broadband detection covering from 300 to 1000 nm and photon-to-electricity conversion efficiencies in excess of 100%.[2] To obtain narrowband photodetection with inorganic-based photodiodes (such as silicon), a filter must be integrated. The use of external optical filters increases system sophistication and limits the integration of PDs in arrays, while increasing manufacturing costs.[3] On the contrary, organic

Q. Eynaud, M. Kramdi, V. Kannampalli, L. Santinacci, J. Ackermann, C. Videlot-Ackermann
Molecular Engineering and Functional Materials Department; NanoMaterials Department
Aix Marseille University
CNRS
CINaM
Marseille 13288, France
E-mail: christine.videlot-ackermann@cnrs.fr

The ORCID identification number(s) for the author(s) of this article can be found under https://doi.org/10.1002/aesr.202300262.

DOI: 10.1002/aesr.202300262

T. Koganezawa
Industrial Application Division
Japan Synchrotron Radiation Research Institute (JASRI)
Sayo, Hyogo 679-5198, Japan

N. Yoshimoto
Department of Physical Science and Materials Engineering
Iwate University
Ueda, Morioka 020 8551, Japan

semiconductors have a wide range of properties that make them ideally suited to narrowband photodetection. Recently, several studies demonstrate the possibility to access to filter-free narrowband photodetection by using organic PDs (OPDs). OPDs are photodiode type (PD–OPDs) with external quantum efficiency (EQE) less than 100% or photomultiplication type (PM–OPDs) with EQE higher than 100%. To achieve selected color discrimination excluding the use of a filter, different mechanisms have been implemented as charge collection narrowing (CCN),[4] charge injection narrowing,[5] exciton dissociation narrowing,[6] or internal light depletion.[7] The CCN mechanism is a new way of controlling the spectral response, with a special feature in that the detection window can be selected to match the absorption onset of the junction materials. Such as solar cells, bulk heterojunctions (BHJs) have been applied to achieve high-efficiency CCN-based OPDs.[4a,8] BHJ enables to overcome the limitation of the short exciton diffusion length in organic materials (≈10 nm). In contrast to planar junctions where this short exciton diffusion length limits the thickness and therefore results in low photocurrents due to insufficient absorption of the incident photons, this short exciton diffusion length can, in contrast, be beneficial for obtaining narrowband OPDs.

In 2015, Armin et al. first developed high-performance CCN-based OPDs using an ultra-thick (2 μm) BHJ active layer.[4a] The authors were able to apply the CCN concept to material systems, PCDTBT:$PC_{70}BM$ and DPP–DTT:$PC_{70}BM$, leading to red (675 nm) and near-infrared (NIR) (930 nm) photoresponses with a sub-100 nm full width at half maximum (FWHM) and a maximum EQE value of 18.1% and 8% at a low reverse bias of −1 V, respectively. The special feature of these OPDs relies on the fact that they are blind to visible light, without the need for additional input filtering. In this structure, incoming photons with energy above the optical gap are absorbed close to the illuminated transparent electrode creating excitons in the first tens or hundreds of nanometers of the BHJ layer. Additionally, after charge separation and due to the long transit time for one type of carrier to cross the entire thick film, the electrons and holes photogenerated near this region recombine before the extraction at the opposite reflecting electrode. Incoming photons whose energy is close to or slightly below the optical gap penetrate the device and reach this reflecting electrode. Carrier generation therefore occurs throughout the thick film, and both types of charge carrier are efficiently extracted. In photoresponse spectra, balanced extraction results in a narrow peak located at the absorption onset of the active layer.

Here we discuss relevant trends, highlighting results obtained with PD-type OPDs based on donor:acceptor (D:A) BHJs with fullerenes or non-fullerene acceptors (NFAs) as acceptors following the CCN concept. **Figure 1** summarizes the performances of narrowband OPDs in terms of efficiency (EQE) and spectral bandwidth (FWHM) since the first reported CCN–OPD in 2015. Table S1 (Supporting Information) listed the corresponding data and references. CCN concept strongly depends on the absorption range of the active layer. The detection window can therefore be adjusted according to the absorption onset of the BHJ material system used. By changing the donor polymer in the $PC_{70}BM$-based BHJ, in 2016, Shen et al. obtained an EQE peak at 890 nm with a value greater than 10% at −7 V bias.[9] Nevertheless at −2 V, EQE decreases to 2%–6.5% (see Table S1, Supporting Information). In 2018, Yon et al. reported a blue selective polymer photodiode based on $PC_{60}BM$ as acceptor with an EQE value up to 37.8% at −1 V.[10] However, with an FWHM as high as 203 nm, the narrowband selectivity is no longer retained. In 2020, Lan et al. obtained 34.3% at −2 V with a 2.7 μm thick ternary PTB7-Th:COi8DFIC:$PC_{70}BM$ NIR-absorbing BHJ layer.[7c] With FWHM of 40 nm, these performance metrics belong to the highest values ever reported for fullerene-based CCN–OPDs, but remains the only system based on three organic compounds.

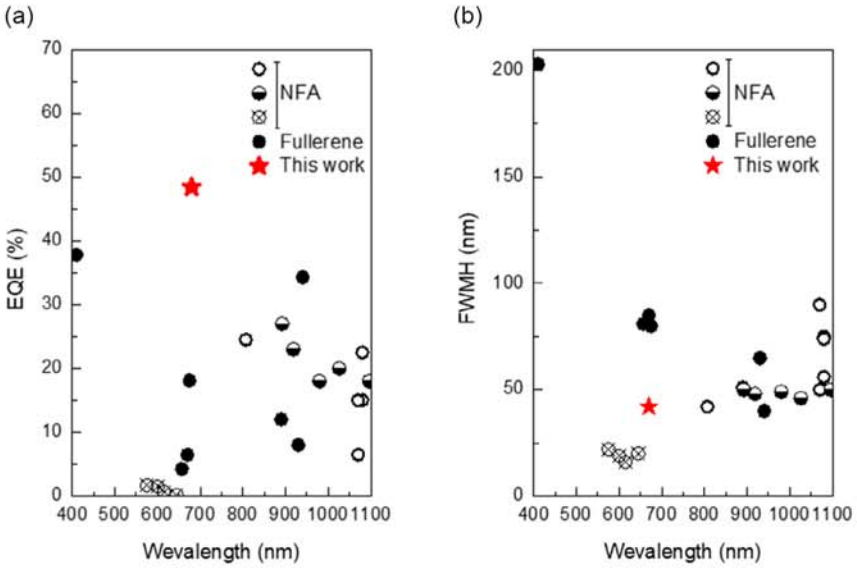

Figure 1. Summary of reported a) EQE and b) FWMH data of charge-collection-narrowing–organic photodetectors (CCN–OPDs) based on BHJ photoactive layers involving nonfullerene acceptor (NFA) or fullerene as acceptors.

In recent years, the development of NFAs led to the rapid emergence of new molecules such as ITIC derivatives, followed by the Y6 family. Compared with fullerenes, the absorption spectra of NFAs have the great advantage of extending into the red and even the NIR, and of being complementary to those of donor polymers. Very recent research has shown the realization of red narrowband OPDs based on NFAs. Liu et al. realized in 2022 efficient NIR selective OPDs (EQE up to 27% and FWHM down to 46 nm).[11] However, theses OPDs remains narrowband only in a selective spectral window (700–1200 nm), as a broad visible band (300–600 nm) is present independently of the applied reverse bias (0, −1, −3, or −5 V). To obtain truly visible-blind narrowband NIR–OPDs, an additional filtering system must be added. The same year, Tsai et al. used new developed donor (PD004) and acceptor (PD-A2) materials to reach self-filtering OPD with a narrowband response at 1080 nm.[8] Despite using extremely thick layers (up to 8.2 µm), the authors reported a single-peak EQE of 53% at −8 V bias, which corresponds to the highest values ever reported in the narrowband IR detection technologies. It is worth noting that the efficiency down by more than half (to 22.5%) at −2 V for the extremely thick OPD and to 15% for a 3.6 µm thick OPD. The same donor polymer blended with a second new synthesized non-fullerene acceptor (NFA) (BTPV-DT-4F) gave rise to an OPD with an EQE value of 15% at −2 V. These devices delivered single peak with FWHM never down to 50 nm at −8 V. Impressive ultra-narrow bandwidth detection (with FWHM of <20 nm) is obtained with CCN–OPDs based on four different helical ribbons that differ in the wavelength of their response; but in contrast, yields of less than 2% are invariably obtained. Recently, Eynaud et al. reported on efficient NFA-based selective NIR OPDs with an external narrowband quantum efficiency of 24.5% and a bandwidth of 42 nm centered at 807 nm.[4d] Based on thick PM6:ITIC-4F BHJ films, the authors demonstrate a filter-free visible-blind NIR-light-responsive characteristic with a high spectral rejection ratio (SRR) of 80.5. This ratio shows the large fraction of the interest peak in comparison with the so-called blind range.

In this work, we report on binary PM6:$PC_{70}BM$ based filter-free OPDs. A fine-tuning over a bandwidth of 42 nm to be highly selective at 677 nm has been reached. In addition to simply being made up of two elements, a donor polymer and a small acceptor molecule, the thickness of the layers has been reduced to less than 2 µm (i.e., 1.6 µm). The optimized OPD exhibits a high-selective spectral response following the CCN principle with an external narrowband quantum efficiency of 48.4% under an inverse low bias of −2 V. The performance metrics (EQE, FWHM) belong to the highest values ever reported for fullerene-based CCN–OPDs (see Figure 1) and exceeds those obtained with the ternary blend by Lan et al.[7c] Since 2015, the development of PD-type OPDs based on BHJs has found new boost thanks to the diversity of materials, both donor and acceptor. Nevertheless, the sustainability of these OPDs is barely mentioned. Using a noninvasive and nondestructive encapsulation technique, we demonstrate that these OPDs fully retain their high selective peak after 30 days storage in air. The filter-free band-selective OPDs have simultaneously a high selectivity, a high responsivity, and a high stability.

2. Performance Metrics of CCN–OPDs

An inverted device geometry was adopted with ZnO and MoO_3 as electron- and hole-transport layers, respectively (**Figure 2**a). Absorption spectra of neat materials (PM6 and $PC_{70}BM$) together with PM6:$PC_{70}BM$ blend film are shown in Figure 2b. While $PC_{70}BM$ demonstrates a strong light absorption in the UV range with a continuously decrease up to 700 nm in the visible region, PM6 absorption is located in the UV–visible region with a maximum between 500 and 800 nm. The absorption spectrum of the PM6:$PC_{70}BM$ blend corresponds well to the addition of the two spectra of the single layers and covers the entire visible absorption range without pronounced minima. On the CCN principle, a photoresponse can be realized by incorporating a thick (1.6 µm) absorbing PM6:$PC_{70}BM$ BHJ layer in the OPD. Figure 2b shows EQE spectra at zero bias (0 V) and reverse bias (−2 V) of PD-type OPDs based on BHJs in 1:1 weight ratio post-annealed at 100 °C. The results demonstrate that our OPDs exhibit a low contribution to the photocurrent from visible wavelengths together with a 677 nm centered narrow peak of 18.8% at 0 V and 48.4% at −2 V, respectively. The CCN-type OPD has a narrowband photoresponse with a 42 nm narrow FWHM. Increased EQE values at

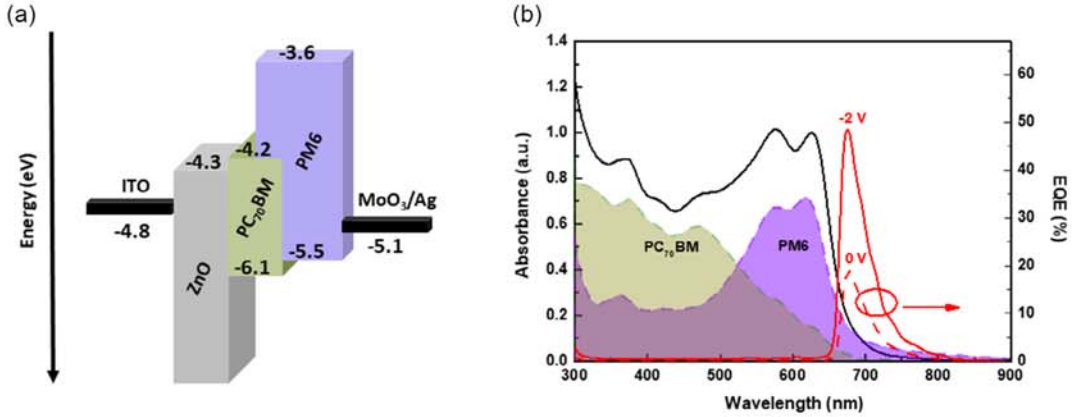

Figure 2. a) Schematic energy diagram of photodiode devices in inverted structure as ITO/ZnO/PM6:$PC_{70}BM$/MoO_3/Ag. b) Normalized UV–vis absorption spectra of neat and blended films (right axe) and EQE spectra of a photodiode device (left axe).

reverse bias is commonly attributed to the enhanced collection of photogenerated charge carriers at large biases.[7c,8,12] The responsivity ($\mathfrak{R}$) of the device is calculated with Equation (1) while SRR with Equation (2) (**Figure 3**a). $\mathfrak{R}$ reaches a maximum value of 263.6 mA W^{-1} at −2 V. This value is comparable to and even slightly higher than that obtained for the ternary PTB7-Th:COi8DFIC:$PC_{70}BM$ NIR-absorbing BHJ layer reported by Lan et al.[7c] In addition, high SRR of 328.6 and 165.1 are obtained at 0 and −2 V, respectively.

Figure 3b shows the current density–voltage (J–V) characteristics measured in dark and under illumination. The devices operate as a photodiode in the dark due to the large energy barrier for charge injection under reverse bias. This can be observed directly by low dark currents in a large reverse bias range, essential for high-performance organic photodiodes. At 0 and −2 V, dark-current density values of ≈12 and ≈20 nA m^{-2} were measured, respectively. Using Equation (3), a specific detectivity D* is calculated as high as 1.62×10^{13} Jones at 0 V (Figure 3c). A slight increase at −2 V is obtained with a value of 3.25×10^{13} Jones due to lower dark current at −2 V. These results in a narrowband photoresponse with a high peak value, a high SRR and a high specific detectivity classify our OPDs as high-performing spectrally selective OPDs.

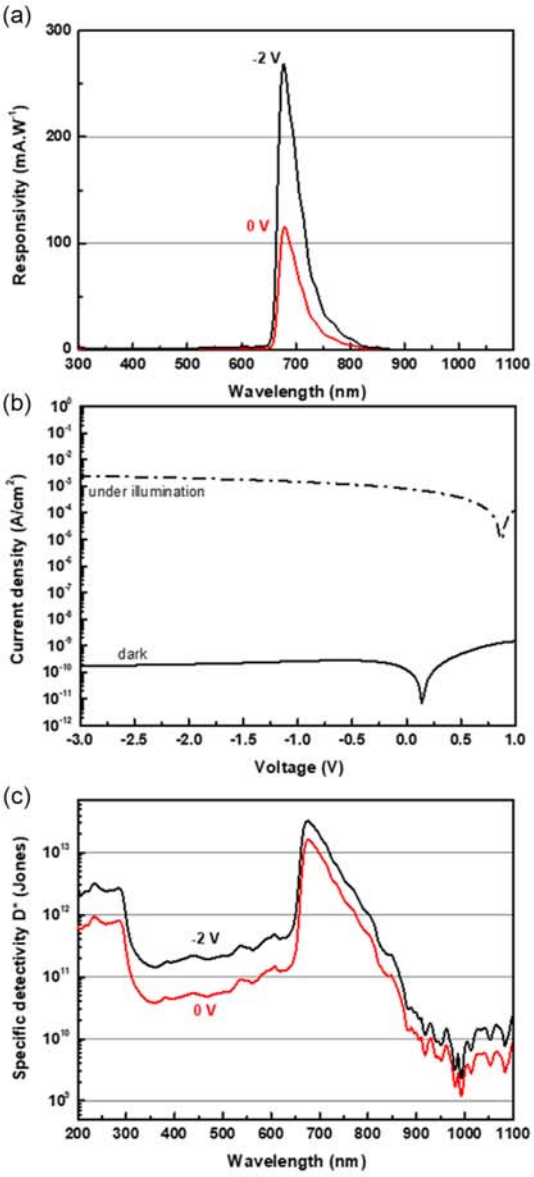

Figure 3. a) Calculated responsivity spectra of the optimized OPD from the EQE measurement at 0 and −2 V. b) Current–voltage characteristics in dark and under light (100 mW cm^{-2}), c) specific detectivity (D*) under 0 and −2 V.

As noted in the literature, some studies reported operating OPDs under high reverse bias (−6, −7, or −8 V) with the principal aim of increasing EQE values. To study the impact of high-applied bias, a CCN-type OPD was dedicated exclusively to this study. The photoresponse of the main peak increases with the reverse bias, i.e., achieving an EQE of 64.7% at −5 V and 87% at −30 V (Figure S1, Supporting Information). This system is therefore very robust to high applied voltage. It is worth noting, however, that the undesired UV–visible light detection (300–600 nm range) also gradually contributes to the photodetection, adding in a visible-light EQE of 46% under −30 V (see Table S2, Supporting Information). An extended detection to the UV–visible light under higher reverse bias deteriorates the band-selective detection capability, leading to a strong overlap by the photons over different wavelength ranges tending toward the photovoltaic effect. Figure S2 (Supporting Information) shows the responsivity $\mathfrak{R}$ spectra measured for the OPD under different reverse biases of 0 up to −30 V with a high responsivity in the 670–680 nm range. The maximum value $\mathfrak{R}$ is 470.6 mA W^{-1} at −30 V. This responsivity is relatively high, as the counter electrode can collect a significant amount of photogenerated charges close to the transparent electrode. However, an excellent SRR (>100) is obtained uniquely for low bias of 0 and −2 V. Although very important for selective OPDs, the SRR parameter is only rarely reported in the literature, and only Lan et al. mention a value of 100 for their ternary OPDs operating at −2 V.[7c]

3. Analysis of PM6:$PC_{70}BM$ Blend Films

X-Ray scattering techniques are extensively used to probe the volume structural state of the blends and to study inner morphology.[4d,13] Particularly in grazing-incidence wide-angle X-Ray scattering (GIWAXS), a very low angle of incidence is applied, ensuring that the beam travels a long way inside the organic film before the data is collected by reflection. The 2D diffraction patterns (q_{xy}, q_z) of blends are shown in **Figure 4**a, together with in-plane (q_{xy}) and out-of-plane (q_z) intensity profiles in Figure 4b. To address peaks to either PM6 or $PC_{70}BM$, neat PM6 layers were analyzed as references (Figure S3 and Table S3, Supporting Information). The emergence of an intense, narrow diffraction peak indexed (100) at $q_z = 0.327$ Å^{-1} in q_z profile highlights that PM6 films are composed of highly ordered crystallites. It is attributed to the edge-on lamellar stacking of PM6 with a lattice constant (d-spacing) of 1.92 nm and a crystal coherence length (CCL) calculated with Equation (4) of 1.10 nm. This typical diffraction peak (100) is also visible in q_{xy} profile, but with a considerably lower intensity, revealing that a very small proportion of PM6 crystallites are oriented with a face-on lamellar stacking. In line

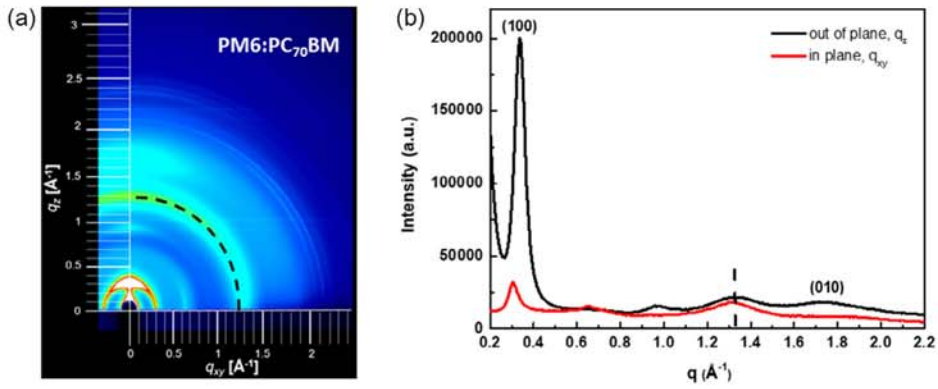

Figure 4. a) The 2D-grazing incidence X-ray diffraction (GIXRD) pattern and b) corresponding out-of-plane and in-plane profiles of PM6:$PC_{70}BM$ blend layers deposited on ZnO buffer layer. The dotted lines in pattern and profiles highlight the $PC_{70}BM$ phase.

with the predominant edge-on molecular orientation of PM6 chains with respect to the substrate, the q_{xy} profile shows a weak (010) peak at 1.73 $Å^{-1}$ corresponding to a π–π stacking with a d spacing of 3.63 nm. Blended with $PC_{70}BM$ in thick BHJ films, the crystalline state of PM6 is conserved as observed by the predominant presence of the diffraction peaks (100) in the q_z profile (Figure 4b). For PM6:$PC_{70}BM$ blend, a reduced d spacing (1.86 nm) together with increased crystallite sizes (1.47 nm) is observed. Due to the addition of the acceptor in the PM6:$PC_{70}BM$ blend, the polymer chains form slightly denser and narrower domains without the formation of larger donor-enriched domains. Furthermore, the presence of $PC_{70}BM$ is clearly visible in blend with a peak at 1.32 $Å^{-1}$ in both profiles, in the form of a ring confirming an amorphous phase of $PC_{70}BM$ in thick BHJ film, highlighting a well intermixing of compounds in a bi-continuous interconnected network. It is widely accepted that this fullerene phase, with no significant aggregation and no formation of oversized domains, will be favorable to OPD performance and stability.

The charge-transport properties of the PM6:$PC_{70}BM$ (1:1 weight ratio) blend films were determined by space-charge-limited current (SCLC).[14] Hole-only and electron-only devices have been realized. Current–voltage (I–V) curves were fitted using Equation (5) in the SCLC region considering a field dependence of the mobility (Figure S4, Supporting Information). Hole (μ_h) and electron (μ_e) mobility values obtained for PM6:$PC_{70}BM$ BHJ layers together with the values of thicknesses are summarized in Table S4 (Supporting Information). Average hole and electron mobility values of 2.48×10^{-3} and 7.26×10^{-4} $cm^2\,Vs^{-1}$ are measured, respectively. These results highlight the huge ability of both charges to be mobile into the bi-continuous network. In addition, thanks to higher charge mobility values, holes that have to pass through the active layer thickness in the inverted OPD configuration can be efficiently collected toward their extracted reflecting electrode.

The CCN concept requires largely imbalanced charge carrier transport, frequently attained by increasing the drift distance of one type of carriers in ultra-thick-based OPD devices. As a generic approach for all material systems, a blend thickness greater than 2 µm will quickly limit its implementation via solution process as spin-coating or doctor-blading techniques. Reducing this thickness to a few hundred nanometers is therefore of key strategic importance. However, this reduction must not be at the expense of dark and noise current level, the FWHM, and the EQE value. Previous reported fullerenes-based OPDs have been fabricated with thin active layers (320–550 nm), but in these circumstances, the FWHM remained very high (81–203 nm) resulting in a loss of selectivity and even, in some cases, a loss of efficiency.[10,15] A compromise is therefore needed between thickness and performances metric for CCN–OPDs. With a 1.6 µm thick OPDs, fully performed narrowband PDs has been achieved here with PM6:$PC_{70}BM$ BHJ layers.

4. Stability of PM6:$PC_{70}BM$-Based OPDs

Even though OPDs have made promising progress in terms of performance and multifunctionality, the required stability of the device remains a precondition for commercial applications. However, while the very few reports on OPD degradation refer to broadband OPDs, an unique study has been carried out on the photostability of OPDs based on the CNN concept.[8] A transition from a narrowband to a broadband response was observed after exposure of nonencapsulated OPDs to light (AM1.5G, 100 mW cm^{-2}) for 63 h, the reason advanced by the authors was a heat-induced change in morphology. We can easily control the working environment, including water, oxygen, and heat via encapsulation. To this purpose, a noninvasive and nondestructive encapsulation technique was used, based on the atomic layer deposition (ALD) method to assess the lifetime of the CCN–OPD.

ALD is a vapor-deposition technique that enables the deposition of high-quality, uniform, and conformal thin films at relatively low temperatures. The special feature of ALD is that it is a surface-controlled layer-by-layer deposition process, enabling thin films to be deposited one atomic layer at a time. These exceptional properties can be used to address the challenges posed by the processing of various types of opto-electronic devices as solar cells. In recent years, academic and industrial research has focused on the application of ALD technology to the photovoltaic industry. ALD films are also excellent barriers to moisture permeation and have been successfully used to

encapsulate flexible copper indium gallium selenide (CIGS) and organic photovoltaic (OPV) cells.[16] To counteract the absence of a single material layer having ultrahigh barrier capability, excellent chemical stability, good mechanical resistance, and high transmittance, multilayer barriers have been successfully explored in ALD. In the present study, an Al_2O_3/TiO_2 bilayer has been realized by ALD for use as an encapsulation material, since the combination of alumina and TiO_2 has been reported to be highly protective.[17] In this bilayer, alumina contributes its exceptional gas-barrier properties, while the TiO_2 layers are perfectly pinhole free under optimized deposition conditions.[18]

Figure S5a (Supporting Information) shows the responsivity spectra of the OPD before and after encapsulation at 0 and −2 V. Encapsulated devices exhibit identical performance metrics, in terms of extremely narrow bandwidth and efficiency, demonstrating the nondestructive property of ALD. The OPDs were first aged in the inert atmosphere in glove box at room temperature (RT) during 27 days. Figure S5b (Supporting Information) shows no change either in target wavelength or in responsivity ($\mathfrak{R}_{max}$) at 0 or −2 V. The very high selectivity of OPDs is retained. The thin Al_2O_3/TiO_2 bilayer (10/10 nm) deposited by ALD causes no deterioration in charge collection. Second, the lifetime of the encapsulated CCN–OPD was achieved by aging in air at RT under laboratory light illumination. As a reference, unencapsulated CCN–OPDs were exposed to the same conditions. **Figure 5**a compares the spectral responses after 30 days of air exposure. While unencapsulated devices exhibit an unexpected result from narrowband to broadband at either 0 or −2 V, encapsulated CCN–OPDs conserve their high-performing selectivity. Figure S6 (Supporting Information) confirms the initial narrowband spectral response of the unencapsulated OPD. Figure 5b tracks the follow-up of the target responsivity value ($\mathfrak{R}_{max}$) and its wavelength (λ_{max}) during the experimental one month period. When exposed to light and ambient conditions, the highly selective peak centered around 674 nm of unencapsulated devices is no longer pronounced, leaving instead a broad spectrum between 300 and 700 nm, as a solar cell based on a 100 nm thin PM6:PC_{70}BM blend (Figure S6, Supporting Information). Although the thickness of the active layer remains constant, OPDs will no longer behave as optically and electrically thick PD-type OPDs.[4c]

Shortly after their first use as acceptors in optoelectronic devices, fullerenes and derivatives were recognized for their sensitivity to photoinduced reactions.[19] In the presence of oxygen, PCBM and derivatives have been shown to undergo photooxidation, with two most commonly observed products of photooxidation, epoxide and carbonyl, on the fullerene cage acting as electron traps.[20] Specifically, electron mobility decreases by two orders of magnitude when a small amount of photooxidized PCBM (weight fraction 3.6%) is present in blend layers. It is important to note that even exposure to conditions typical of laboratory environments (low light intensity, air) is sufficient to induce photooxidation of fullerenes in fullerene-based BHJ.[20c] For our BHJ system, the transition from a narrowband to a broadband response of the devices after long time storage in the air is illustrated in **Figure 6**. At the initial stage of air exposure (t_0), the detection follows the Beer–Lambert law assigned to CCN–OPDs. Photons with energy corresponding to the absorption peak of materials will be absorbed in the light-penetration area to generate photo-carriers. Due to the low mobility of holes and the thickness of the active layer, they recombine before collecting at the Ag electrode (case (1) in Figure 6a. Photons whose energy is close to the absorption tail can penetrate deeper into the active layer leading to a uniform generation and collection of charges (case (2) in Figure 6a). In the EQE spectrum, this ideally translates into a specific photoresponse and blindness outside this spectral window. After 30 days of exposure to air, the consequences of photooxidation of fullerene molecules are directly visible on the EQE spectrum profile (Figure 6b). Photon absorption and charge generation are based on the same mechanisms as at t_0, but the outcome of these charges differs. In case (2) in Figure 6b, the electrons will be negatively affected by their reduced mobility and traps. As a result, electrons are trapped before they reach their collecting electrode, eliminating the CCN peak in the EQE spectrum. In the case of photons absorb in the absorption peak of materials (case (1) in Figure 6b), electrons and holes will be generated within the light penetration range. Electrons generated near their extraction electrode can

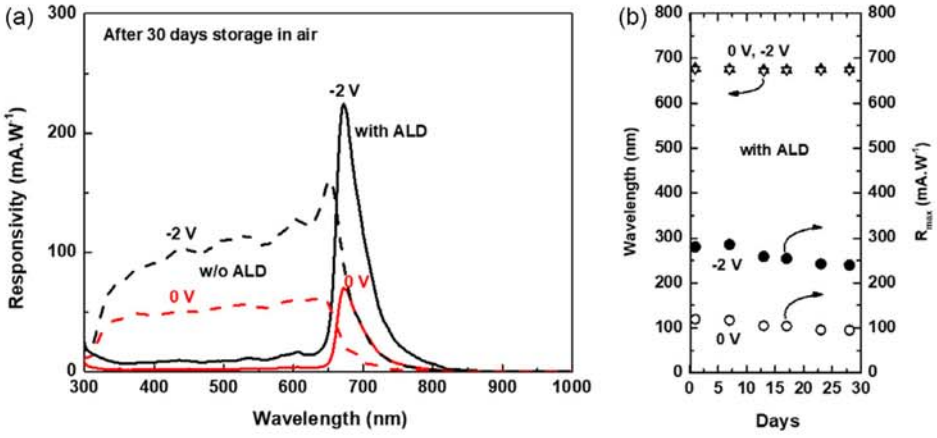

Figure 5. a) Responsivity spectra of encapsulated (full lines) and unencapsulated (dashed lines) OPDs at 0 and −2 V after 30 days storage in air. b) Time evolution of the target wavelength and its responsivity value ($\mathfrak{R}_{max}$) of encapsulated OPD with atomic layer deposition (ALD) after 30 days storage in air.

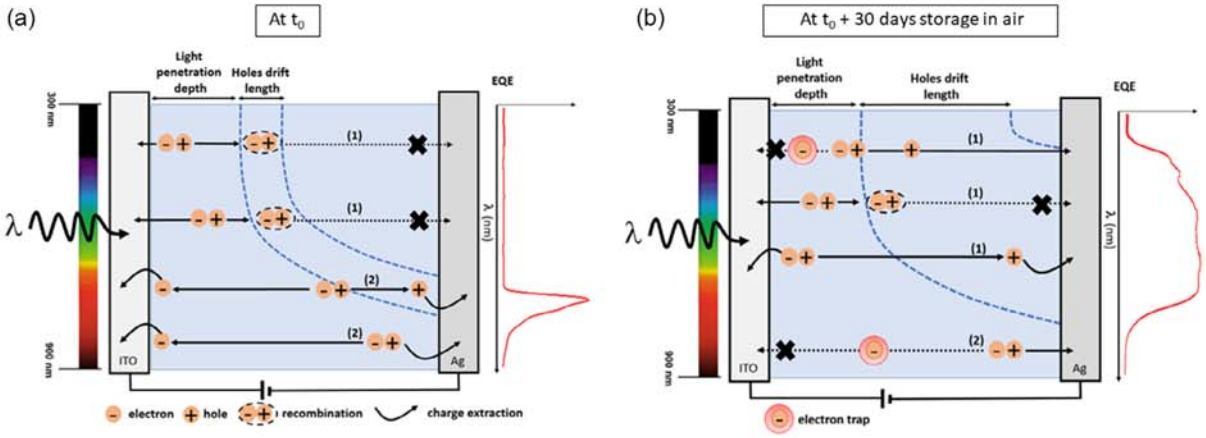

Figure 6. Schematic representation of the operating principle of OPDs based on 1.6 µm thick PM6:$PC_{70}BM$ BHJ films just after their conception (t_0) in (a) and after 30 days of exposure in air ($t_0 + 30$ days) in (b).

be collected, while those generated further inside the light penetration area will be exposed to trapping. The presence of electron traps directly reduces the electron collection rate, but also the charge recombination rate, which is beneficial for the hole outcome. The hole drift length will be extended to their extraction electrode through the blend layer, allowing efficient hole collection. Consequently, electrons and holes are collected at the front (illuminated transparent indium tin oxide (ITO) electrode) and back electrodes (Ag electrode), respectively, to give rise to broadband EQE spectra, corresponding to the absorption spectra of blend materials. It is worth noting, however, that EQE values will never be as high as obtained for an OPV cells (Figure S6, Supporting Information) due to losses associated to electron traps and charge recombination.

Several factors affect the stability of OPDs, including thermal stress, light-induced photodegradation, O_2/H_2O exposure, electric field, and device structure.[21] In our case, several of these factors can be ruled out as being at the origin of the transition, where only the effect of O_2/H_2O exposure remains unavoidable in unencapsulated OPDs. This further indicates that the entry of H_2O and O_2 in the atmosphere is the first cause of degradation, and that the ALD-treated Al_2O_3/TiO_2 bilayer is therefore an effective barrier layer.

5. Conclusion

We demonstrate high-performance filter-free visible-blind OPDs utilizing the CCN effect originated from a 1.6 µm thick PM6:$PC_{70}BM$ BHJ film. A well-mixed, bi-continuous D:A morphology in thick films, essential for efficient carrier generation and transport, is highlighted by GIWAXS. Whereas until now, organic-based CCN devices have EQEs generally not higher than ≈40%, and a single-peak EQE response of 48.4% at a centered wavelength at 677 nm, along with a narrow FWHM of 42 nm, is obtained. A specific detectivity D* over 10^{12}–10^{13} Jones due to low dark currents are obtained. In addition, using a noninvasive and nondestructive encapsulation technique by ALD, we demonstrate that these filter-free band-selective OPDs fully retain their high selectivity and their high responsivity, to be highly stable in air. All these performance metrics can pave the way for commercial applications and highlighted the great potential of achieving highly stable OPDs with fullerene or NFA as acceptors.

6. Experimental Section

Materials: Patterned ITO substrates (size of 25 × 25 mm) with 15 Ω sq^{-1} resistance were purchased from Lumtec, Taiwan. A 2.5 vol% ZnO nanoparticle solution in alcohol-blended ZnO was purchased from Avantama and diluted to 1 vol% before use. O-xylene, 1,2,3,4-tetrahydronaphthalene (tetralin), and molybdenum (VI) oxide (MoO_3 purity 99.97%) were purchased from Sigma-Aldrich. PM6 (Mw≈120 kDa; polydispersity index (PDI) 3.0) and $PC_{70}BM$ were purchased from 1-Material and Nano-C, respectively. Aluminum (Al, purity 99.999%) and silver (Ag, purity 99.99%) were purchased from Kurt J. Lesker. Lithium fluoride powder (LiF, purity ≥ 99.99%) was purchased from Sigma-Aldrich (Merck). All commercial materials were used as received without purification and kept under nitrogen atmosphere.

OPDs Fabrication: The PDs were fabricated in inverted (ITO/ZnO/PM6:$PC_{70}BM$/MoO_3/Ag) structure on ITO-coated glasses using spin-coating technique in glove box under nitrogen atmosphere. First, the ITO substrates were thoroughly cleaned with clean cloth dampened with isopropanol before sonication in isopropanol for 30 min and applying UV ozone for 15 min at 80 °C. A thin layer of ZnO was spin-coated on the cleaned ITO substrate in the ambient conditions at a speed of 5000 rpm for 60 s followed by an annealing step inside nitrogen-filled glove box at 100 °C for 10 min to form 15 nm thick film. A PM6:$PC_{70}BM$ blend solution (1:1 weight ratio at 30–40 mg mL^{-1}) for the photoactive layer were used in (95% volume) o-xylene and (5% volume) tetralin. Inks have been stirred at 80 °C overnight. PM6:$PC_{70}BM$ layers were spin-coated inside nitrogen-filled glove box at 800 rpm for 120 s following by a post-deposition thermal annealing at 100 °C for 10 min. MoO_3 and Ag were successively thermally evaporated at 2×10^{-6} mbar to 2 and 100 nm thick layers, respectively, using a shadow mask to obtain device areas of 0.09 and 0.25 cm^2.

The PDs were encapsulated by Al_2O_3 and TiO_2 thin films grown by ALD to protect the device surface from the damaging effects of atmospheric exposure similarly to previous work to protect plasmonic systems.[22] ALD was carried out in a Fiji 200 reactor (Veeco/Cambridge Nanotech) operating with Ar gas carrier.[18,23] In both cases, the reaction chamber was maintained at 90 °C. Al_2O_3 was deposited from trimethylaluminum (TMA from Strem Chemicals, 98%) and deionized water ($\rho = 18.2$ MΩ cm) that were stored in dedicated canisters at RT. The

ALD cycle consisted of sequential pulses and purges of TMA and H_2O, alternatively. The pulse and purge durations were 0.06:10 s for both precursors. TiO_2 films were grown from tetrakis(dimethylamino)titanium (TDMAT, Strem Chemicals, 99%) and deionized water by thermal ALD. TDMAT was maintained at 85 °C and water was left at RT. The ALD cycle consisted of sequential pulses, exposures, and purges of both TDMAT and H_2O, alternatively. The pulse, exposure, and purge durations were 1:7:15 s for the Ti precursor and 0.2:7:15 s for water. The number of ALD cycles were adjusted according to the growth per cycle (GPC) of each process (GPC = 0.8 and 0.6 Å cycle^{-1}) to end up with an Al_2O_3/TiO_2 bilayer exhibiting a thickness of 10/10 nm, respectively.

OPDs Characterization: The dark *J–V* characteristics of the devices were measured in a light occulting Faraday cage inside the glove box using a Keithley 238 Source Measure Unit allowing to measure tens of femtoamperes. The 1 m triax leads were used to minimize the measurement noise. The same setup was used for light *J–V* measurements with devices out from Faraday cage to be exposed to a Newport solar simulator (Sol3A Class AAA, IEC/JIS/ASTM, 450 W Xenon, 4 × 4 in Model: 94043A) with an irradiation intensity of 100 mW cm^{-2}. The light intensity was determined with a Si reference cell (Newport Company 2 × 2 cm calibrated solar cell made of monocrystalline silicon and a fused silica window Model: 91150V) calibrated by the National Renewable Energy Laboratory (NREL). EQE measurements were processed in a dark room in ambient conditions with a 150 W Xe arc lamp Apex illuminator (70 525) light source collimated to a Cornerstone 260 1/4 m UV–VIS Monochromator (74 125) from Oriel Instruments for the light part and with a Keithley 238 Source Measure Unit for the electrical part. Devices were mounted on an optical table in a Faraday cage with an aperture to expose the samples to the monochromatic light. The electrodes of the devices were electrically connected to the cage by spring-loaded pogo pin connectors. The light beam was filtrated with 295 nm (10CGA-295) and 570 nm (10CGA-570) long-pass filters before reaching the devices. Light The responsivity $\mathfrak{R}$ was calculated from the EQE spectra, using the following equation:

$$\mathfrak{R} = \frac{J_{ph} - J_d}{L_{opt(\lambda)}} \approx \frac{J_{ph}}{L_{opt(\lambda)}} = EQE.\frac{\lambda q}{hc} \quad (1)$$

where J_{ph} is the current density under illumination, in mA cm^{-2}, and L_{opt} is the incident light power density, in mW cm^{-2}. J_d is the dark-current density and is extremely small as compared to J_{ph} and therefore can be neglected.[24]

The cross talk of the OPD over different spectral regions could be described using the SRR, defined as the ratio of the responsivity at the target wavelength to the one at the untargeted reference wavelength (here 460 nm). SRR can be calculated by

$$SRR = \frac{\mathfrak{R}(\lambda_{target})}{\mathfrak{R}(\lambda_{460})} \quad (2)$$

where λ_{target} is the wavelength of the light within the detection spectral range (i.e., maximum EQE peak) and λ_{460} is the wavelength of the light outside the detection spectral range (i.e., 460 nm in the present study).

Assuming that for OPDs in which a reverse bias was applied, the dark-current shot noise was considered the dominant contribution, the specific detectivity (D*) could be expressed as follows:[24,25]

$$D^* = \frac{\mathfrak{R}}{\sqrt{2qJ_d}} \quad (3)$$

where q is elementary charge and J_d is the dark-current density in A cm^{-2}.

Characterization of Organic Films: The absorbance of the active layer films was measured by UV–vis–NIR Spectrophotometer Cary 5000. Film thicknesses were measured by a stylus profilometer (Bruker DEKTAK XT) with 1 mg force on the probing tip.

Thin films were further analyzed with high-brightness synchrotron radiation at BL19B2 in SPring-8 (Japan). GIWAXS measurements were performed using a high-sensitive 2D X-Ray detector (PILATUS 300 K). The incident angle and wavelength of X-rays were 0.13° and 0.100 nm, respectively. The CCL values were extracted by the Scherrer equation:

$$\tau = \frac{K\lambda}{\beta\cos\theta} \quad (4)$$

where τ is the ordered (crystalline) domain's mean size, here defined as CCL, K is a constant (dimensionless shape factor) closed to unity. The shape factor is typically equal to 0.9, λ is the wavelength of the X-Ray, β is the FWHM of the diffraction peak in radians after subtracting the instrumental line broadening and θ is the Bragg angle.

Fabrication and Measurements of Space-Charge-Limited Current Devices: SCLC devices required careful choice of the contacts to ensure sufficient injection of the desired carrier, and effective blocking of the other carrier to work like single-carrier devices.[26] Hole-only and electron-only devices consisted of ITO/PEDOT:PSS/PM6:$PC_{70}BM$/MoO_3/Au and ITO/ZnO/PM6:$PC_{70}BM$/LiF/Al, respectively. In SCLC-based devices, the mobility was measured vertically in the entire bulk of the active layer sandwiched between the two interfacial layers. Top metallic electrodes were thermally evaporated (MBRAUN evaporator inside the glove box) at 2 × 10^{-6} mbar to a controlled thickness (13 nm of MoO_3, 100 nm Au, 0.5 nm LiF and 100 nm of Al) using a shadow mask that defines the device areas to 0.09 or 0.25 cm^2 and allows a four-probe measurement. SCLC four-probe measurements were done in the same Faraday cage as for OPDs inside the glove box. The pristine PM6:$PC_{70}BM$ (1:1 ratio, at concentration of 20 mg mL^{-1}) solution was deposited by spin-coating at 1000 rpm for 60 s. Active layers were subsequently annealed at 100 °C during 10 min. The thicknesses of films were measured precisely with a DEKTAK XT profilometer from Bruker.

The measured dark current was fitted using the Murgatroyd expression:

$$I = A\mu_0\frac{9}{8}\frac{V^2}{d^3}\varepsilon\varepsilon_0\exp\left(0.891\gamma\sqrt{\frac{V}{d}}\right) \quad (5)$$

where d is the active layer thickness, A is the active device area, $\varepsilon\varepsilon_0$ is the permittivity of the active layer (ε is assumed equal to 3.5 and ε_0 is the permittivity of free space), and V is the voltage. μ_0 and γ are the unknown parameters that will be adjusted to get a good fit, all other parameters are fixed. μ_0 is the mobility at low electric fields, and γ is a parameter that represents the field dependence of mobility.[14]

Supporting Information

Supporting Information is available from the Wiley Online Library or from the author.

Acknowledgements

This project has received funding by the French Research Agency (project ANR-18-CE04-0007-04 named BELUGA and project ANR-22-CE06-0018 named MONOPOLY). The synchrotron radiation experiments were performed at BL19B2 in Spring-8 with the approval of Japan Synchrotron Radiation Research Institute (JASRI) (Proposal No. 2022A2069 and 2022A2063). C.V.A. and J.A thank F. Jandard and S. Lavandier from CINaM (Electronics and instrumentation division) for their assistance in building the OPD measurement facilities and developing the acquisition software.

Conflict of Interest

The authors declare no conflict of interest.

Data Availability Statement

The data that support the findings of this study are available from the corresponding author upon reasonable request.

Keywords

bulk heterojunctions, charge collection narrowing, encapsulation, filter-free, organic photodetectors, selectivity, stability

Received: November 14, 2023
Revised: December 6, 2023
Published online:

[1] (a) J. H. Kim, A. Liess, M. Stolte, A.-M. Krause, V. Stepanenko, C. Zhong, D. Bialas, F. Spano, F. Würthner, *Adv. Mater.* **2021**, *33*, 2100582; (b) Z. J. Lan, M. H. Lee, F. R. Zhu, *Adv. Intell. Syst.* **2022**, *4*, 2100167; (c) Y. Z. Wang, J. Kublitski, S. Xing, F. Dollinger, D. Spoltore, J. Benduhn, K. Leo, *Mater. Horiz.* **2022**, *9*, 220.

[2] (a) M. Liu, Q. Fan, K. Yang, Z. Zhao, X. Zhao, Z. Zhou, J. Zhang, F. Lin, A. K.-Y. Jen, F. Zhang, *Sci. China Chem.* **2022**, *65*, 1642; (b) K. Yang, Z. Zhao, M. Liu, L. Niu, X. Zhao, G. Yuan, X. Ma, F. Zhang, *J. Mater. Chem. C* **2022**, *10*, 10888.

[3] R. Lukac, *J. Real-Time Image Process.* **2006**, *1*, 45.

[4] (a) A. Armin, R. D. Jansen-van Vuuren, N. Kopidakis, P. L. Burn, P. Meredith, *Nat. Commun.* **2015**, *6*, 6343; (b) A. Armin, A. Yazmaciyan, M. Hambsch, J. Li, P. L. Burn, P. Meredith, *ACS Photonics* **2015**, *2*, 1745; (c) A. Yazmaciyan, P. Meredith, A. Armin, *Adv. Optical Mater.* **2019**, 1801543; (d) Q. Eynaud, Y. A. Avalos Quiroz, T. Koganezawa, R. Sato, N. Yoshimoto, O. Margeat, C. M. Ruiz, J. Ackermann, C. Videlot-Ackermann, *J. Mater. Chem. C* **2023**, *11*, 9657.

[5] (a) W. B. Wang, F. J. Zhang, M. D. Du, L. L. Li, M. Zhang, K. Wang, Y. S. Wang, B. Hu, Y. Fang, J. S. Huang, *Nano Lett.* **2017**, *17*, 1995; (b) J. Miao, F. Zhang, M. Du, W. Wang, Y. Fang, *Phys. Chem. Chem. Phys.* **2017**, *19*, 14424; (c) J. Miao, F. Zhang, M. Du, W. Wang, Y. Fang, *Adv. Optical Mater.* **2018**, *6*, 1800001; (d) W. Wang, M. Du, M. Zhang, J. Miao, Y. Fang, F. Zhang, *Adv. Optical Mater.* **2018**, *6*, 1800249; (e) Z. Zhao, C. Xu, Y. Ma, X. Ma, X. Zhu, L. Niu, L. Shen, Z. Zhou, F. Zhang, *Adv. Funct. Mater.* **2023**, *33*, 2212149.

[6] B. M. Xie, R. H. Xie, K. Zhang, Q. W. Yin, Z. C. Hu, G. Yu, F. Huang, Y. Cao, *Nat. Commun.* **2020**, *11*, 2871.

[7] (a) K. M. Sim, S. Yoon, J. Cho, M. S. Jang, D. S. Chung, *ACS Appl. Mater. Interfaces* **2018**, *10*, 8405; (b) J. Kim, S. Yoon, K. M. Sim, D. S. Chung, *J. Mater. Chem. C* **2019**, *7*, 4770; (c) Z. J. Lan, Y. S. Lau, Y. W. Wang, Z. Xiao, L. M. Ding, D. Luo, F. R. Zhu, *Adv. Opt. Mater.* **2020**, *8*, 20001308.

[8] K. W. Tsai, G. Madhaiyan, L. H. Lai, Y. T. Hsiao, J. L. Wu, C. Y. Liao, C. H. Hou, J. J. Shyue, Y. M. Chang, *ACS Appl. Mater. Interfaces* **2022**, *14*, 38004.

[9] (a) L. Shen, Y. Zhang, Y. Bai, X. Zheng, Q. Wang, J. Huang, *Nanoscale* **2016**, *8*, 12990; (b) L. Shen, Y. Fang, H. Wei, Y. Yuan, J. Huang, *Adv. Mater.* **2016**, *28*, 2043.

[10] S. Yoon, Y. H. Ha, S. K. Kwon, Y. H. Kim, D. S. Chung, *ACS Photonics* **2018**, *5*, 636.

[11] Q. Liu, S. Zeiske, X. Jiang, D. Desta, S. Mertens, S. Gielen, R. Shanivarasanthe, H. G. Boyen, A. Armin, K. Vandewal, *Nat. Commun.* **2022**, *13*, 5194.

[12] H. Bristow, P. Jacoutot, A. D. Scaccabarozzi, M. Babics, M. Moser, A. Wadsworth, T. D. Anthopoulos, A. Bakulin, I. McCulloch, N. Gasparini, *ACS Appl. Mater. Interfaces* **2020**, *12*, 48836.

[13] A. Mahmood, J.-L. Wang, *Sol. RRL* **2020**, *4*, 2000337.

[14] J. C. Blakesley, F. A. Castro, W. Kylberg, G. F. A. Dibb, C. Arantes, R. Valaski, M. Cremona, J. S. Kim, J.-S. Kim, *Org. Electron.* **2014**, *15*, 1263.

[15] S. K. Kim, S. Park, H. J. Son, D. S. Chung, *Macromolecules* **2018**, *51*, 8241.

[16] J. A. van Delft, D. Garcia-Alonso, W. M. M. Kessels, *Semicond. Sci. Technol.* **2012**, *27*, 074002.

[17] A. I. Abdulagatov, Y. Yan, J. R. Cooper, Y. Zhang, Z. M. Gibbs, A. S. Cavanagh, R. G. Yang, Y. C. Lee, S. M. George, *ACS Appl. Mater. Interfaces* **2011**, *3*, 4593.

[18] M. E. Dufond, M. W. Diouf, C. Badie, C. Laffon, P. Parent, D. Ferry, D. Grosso, J. C. S. Kools, S. D. Elliott, L. Santinacci, *Chem. Mater.* **2020**, *32*, 1393.

[19] (a) A. M. Rao, P. Zhou, K.-A. Wang, G. T. Hager, J. M. Holden, Y. Wang, W.-T. Lee, X.-X. Bi, P. C. Eklund, D. S. Cornett, M. A. Duncan, I. J. Amster, *Science* **1993**, *259*, 955; (b) P. C. Eklund, A. M. Rao, P. Zhou, Y. Wang, J. M. Holden, *Thin Solid Films* **1995**, *257*, 185.

[20] (a) S. Yamane, J. Mizukado, Y. Suzuki, M. Sakurai, L. Chen, H. Suda, *Chem. Lett.* **2015**, *44*, 339; (b) Z. Xiao, J. Yao, D. Yang, F. Wang, S. Huang, L. Gan, Z. Jia, Z. Jiang, X. Yang, B. Zheng, G. Yuan, S. Zhang, Z. Wang, *J. Am. Chem. Soc.* **2007**, *129*, 16149; (c) H. K. H. Lee, A. M. Telford, J. A. Röhr, M. F. Wyatt, B. Rice, J. Wu, A. de Castro Maciel, S. M. Tuladhar, E. Speller, J. McGettrick, J. R. Searle, S. Pont, T. Watson, T. Kirchartz, J. R. Durrant, W. C. Tsoi, J. Nelson, Z. Li, *Energy Environ. Sci.* **2018**, *11*, 417.

[21] B.-H. Jiang, D.-W. Lin, M.-N. Shiu, Y.-W. Su, T.-H. Tsai, P.-H. Tsai, T.-S. Shieh, C. K. Chan, J.-H. Lu, C.-P. Chen, *Adv. Opt. Mater.* **2023**, *11*, 2203129.

[22] R. Prithu, C. Badie, J.-B. Claude, A. Barulin, A. Moreau, J. Lumeau, M. Abbarchi, L. Santinacci, J. Wenger, *ACS Appl. Nano Mater.* **2021**, *4*, 7199.

[23] L. Assaud, M. Hanbücken, L. Santinacci, *ECS Trans.* **2013**, *50*, 151.

[24] M. Kielar, O. Dhez, G. Pecastaings, A. Curutchet, L. Hirsch, *Sci. Rep.* **2016**, *6*, 39201.

[25] (a) X. Liu, Y. Lin, Y. Liao, J. Wu, Y. Zheng, *J. Mater. Chem. C* **2018**, *6*, 3499; (b) T. H. Lee, Y. Dong, R. A. Pacalaj, S. Y. Park, W. Xu, J.-S. Kim, J. R. Durrant, *Adv. Funct. Mater.* **2022**, *32*, 2208001.

[26] S. Ben Dkhil, P. Perkhun, C. Luo, D. Müller, R. Alkarsifi, E. Barulina, Y. A. Avalos Quiroz, O. Margeat, S. T. Dubas, T. Koganezawa, D. Kuzuhara, N. Yoshimoto, C. Caddeo, A. Mattoni, B. Zimmermann, U. Würfel, M. Pfannmöller, S. Bals, J. Ackermann, C. Videlot-Ackermann, *ACS Appl. Mater. Interfaces* **2020**, *12*, 28404.